Laser wavelength effects on the charge state resolved ion energy distributions from laser-produced Sn plasma

Russell A. Burdt,[1,2,a)] Yezheng Tao,[1] Mark S. Tillack,[1] Sam Yuspeh,[1,2] Nek M. Shaikh,[1] Eli Flaxer,[3] and Farrokh Najmabadi[1,2]
[1]*Center for Energy Research, University of California San Diego, La Jolla, California 92093, USA*
[2]*Electrical and Computer Engineering, University of California San Diego, La Jolla, California 92093, USA*
[3]*AFEKA - Tel-Aviv Academic College of Engineering, 69107 Tel-Aviv, Israel*

(Received 2 November 2009; accepted 9 January 2010; published online 22 February 2010)

The effects of laser wavelength on the charge state resolved ion energy distributions from laser-produced Sn plasma freely expanding into vacuum are investigated. Planar Sn targets are irradiated at laser wavelengths of 10.6 and 1.064 μm and intensities of 1.8×10^{10} and 3.4×10^{11} W/cm^2, respectively. These parameters are relevant to the extreme ultraviolet x-ray source application. An electrostatic deflection probe and single channel electron multiplier are used to record the charge state resolved ion energy distributions 100 cm from the laser plasma source. At the longer laser wavelength, higher charge state ions are observed. At both laser wavelengths, the peak ion energies increase approximately linearly as a function of charge state, and all ion energies greatly exceed the initial thermal electron temperature. The differences in the ion energy distributions are attributed to the laser wavelength dependence of the laser energy absorption, the resulting plasma density in the corona, and the subsequent recombination after the laser pulse. Numerical simulations of the plasma expansion from a collisional-radiative steady state model support the experimental results. © *2010 American Institute of Physics*. [doi:10.1063/1.3309413]

I. INTRODUCTION

In the interaction of a solid target and a focused laser with long pulse duration (>1 ns) and moderate intensity ($<10^{15}/\lambda^2$ W/cm^2, where λ is the laser wavelength in μm), a hot and highly ionized plasma is formed at the target surface and the laser energy is absorbed by inverse bremsstrahlung up to the critical density ($n_{cr}[cm^{-3}]\approx10^{21}/\lambda^2$).[1–3] The laser absorption is then more efficient using short wavelength lasers, where the critical density and collision frequency are both large. A laser-produced Sn plasma in this regime with electron temperature of 30–40 eV will emit strongly by an unresolved transition array in the extreme ultraviolet (EUV) spectrum centered at 13.5 nm, and this plasma radiation finds application as a source of soft x-rays for next-generation manufacturing of integrated circuits.[4–6] However, the laser-produced Sn plasma is only useful to the application if it is optically thin to its own 13.5 nm radiation, i.e., if it is not too dense.[7] The opacity requirement then motivates the use of long wavelength lasers that create lower density plasmas. For these reasons, laser-produced Sn plasma using both 10.6 μm CO_2 lasers and 1.064 μm neodymium-doped yttrium aluminum garnet (Nd:YAG) lasers are current topics of interest.

The dynamics of Sn plasma produced by an Nd:YAG laser have been thoroughly investigated.[8–10] The conversion of laser energy to 13.5 nm x-rays in a 2% bandwidth escaping the plasma over 2π sr, a figure of merit in the EUV x-ray source industry referred to as in-band conversion efficiency (CE), reaches an optimal value of approximately 2% at a laser intensity of a few 10^{11} W/cm^2. More recently, the CE of a Sn plasma produced by a CO_2 laser has reached higher values of 3%–4% at laser intensities from 10^9 to 10^{10} W/cm^2.[6,11,12] The high transparency to 13.5 nm radiation of the CO_2 laser-produced plasma (LPP), as compared to the Nd:YAG LPP, offsets the lower laser energy absorption and leads to higher CE. Clearly, other laser wavelength-dependent effects will be exhibited by the Sn plasma.

The effects of laser wavelength on the properties of the ions emitted by the plasma are of particular interest, as the ions are a source of damage to the expensive multilayer Mo/Si optics used to collect and focus the 13.5 nm radiation escaping the plasma for use in the application.[13] Mitigation of ions emitted by laser-produced Sn plasma to levels allowing the Mo/Si optics to meet certain lifetime requirements remains a central problem in the development of an economical EUV x-ray source. Accordingly, many of the previous studies of ions emitted by laser-produced Sn plasma have focused entirely on mitigation schemes, such as electrostatic and magnetostatic fields, and background gases.[14,15] Here, some fundamental properties of the ions as a function of laser wavelength are studied experimentally and numerically for the first time. In particular, the charge state resolved ion energy distributions far away from the laser plasma source are measured in parameter space relevant to the EUV x-ray source application, at laser wavelengths of 10.6 and 1.064 μm and intensities of 1.8×10^{10} and 3.4×10^{11} W/cm^2, respectively.

II. EXPERIMENTAL CONDITIONS AND RESULTS

The experimental arrangement is shown in Fig. 1. A planar Sn target is irradiated in one experiment by an Nd:YAG laser and in another by a CO_2 laser. The experiments are

a)Electronic mail: russellburdt@yahoo.com.

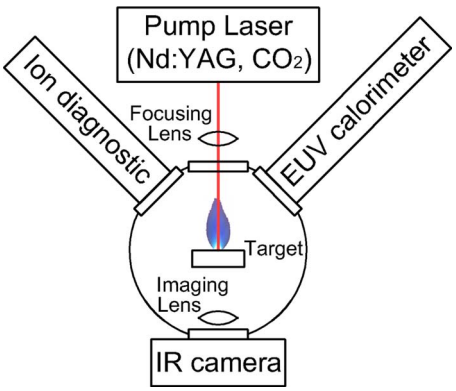

FIG. 1. (Color online) Experimental arrangement. The EUV calorimeter and ion diagnostic are positioned at 45° and 51° with respect to the laser axis, respectively. In the optical path at each laser wavelength, not shown here, were installed a photodiode and laser energy monitor for real-time monitoring of the laser pulse duration and energy. The infrared camera used in the laser focal diameter measurement is a DataRay WinCamD for the Nd:YAG beam and an Ophir–Spiricon PyroCAM III for the CO_2 beam. Images of the CO_2 beam can be found in Ref. 17.

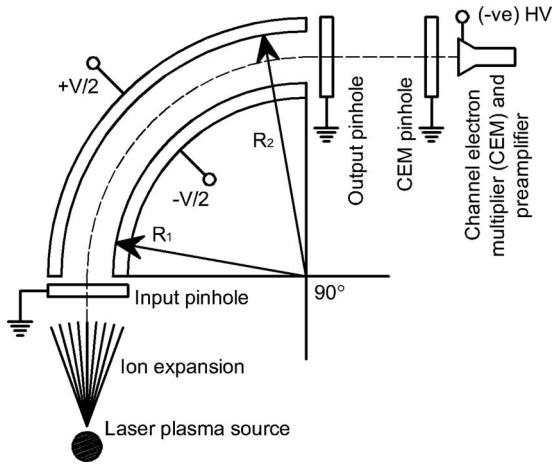

FIG. 2. Diagram of the electrostatic ion energy analyzer. The filter ratio of the probe in electron volt is $KE/Z = V/[2\ln(R_2/R_1)]$, where R_1 and R_2 are the inner and outer radius, respectively, and V is the applied voltage in volts. The CEM is biased to a negative high voltage of 2 kV.

conducted in vacuum below 3×10^{-6} torr so charge-exchange with the ambient will be negligible. The target is translated in the focal plane before each shot to provide a fresh surface. The laser focal diameter is measured by imaging the beam in the focal plane at a known magnification using an appropriate imaging lens and camera for each laser wavelength. The laser and focusing parameters at each wavelength are summarized in Table I. The CE is measured at each laser wavelength with a calibrated EUV calorimeter and is 2% using the Nd:YAG laser and 3% using the CO_2 laser. Additional details on the lasers, beam diagnostics, and the technique used to measure CE have been reported elsewhere.[16,17]

The charge state resolved ion energy distributions are measured with an electrostatic deflection probe and single channel electron multiplier (CEM). This custom-built ion diagnostic, shown schematically in Fig. 2, filters the plasma in a radial electrostatic field into groups of ions having a constant kinetic energy to charge state (KE/Z) ratio, and detects these ions directly with a CEM, similar probes are described in detail elsewhere.[18,19] The laser plasma source must be far enough away from the diagnostic so the effects of space charge expansion on the filtered ion groups is negligible, this distance being 100 cm in the present parameter space.[20] A low noise, high bandwidth, custom-built preamplifier is used at the output of the CEM.[21] The detection efficiency of the CEM, which depends on the energy and mass of the incident ion, is calculated from empirical data in the literature.[22] A typical waveform generated by the ion diagnostic is shown in Fig. 3, in which the individual peaks represent the arrival of Sn ions with varying charge state meeting the filter criterion of the probe, KE/Z=121 eV in this sample. A complete ion energy spectrum can be generated through repetitive experimentation as the filter criterion of the probe is scanned by varying the applied voltage on the cylindrical electrodes.

The charge state resolved ion energy distributions from Nd:YAG and CO_2 LPP are shown in Figs. 4(a) and 4(b), respectively. These data are time-integrated and represent a solid angle of observation of 2.5×10^{-7} sr (a 1 mm input pinhole positioned 100 cm from a small laser plasma source). The data analysis methods used for calculating the ion energy distributions (as seen in Fig. 4) from multiple time-of-flight waveforms (one example is seen in Fig. 3) as the KE/Z ratio is scanned can be found in Woryna *et al.*,[18] here approximately 30 shots under repetitive laser conditions were used in the data analysis at both laser wavelengths.

The ion energy distributions for each charge state at both laser wavelengths are fit in a least squares sense by functions of the form

$$f(E_{\text{ion}}) = AE_{\text{ion}}\exp[-(E_{\text{ion}}-\mu)^2/(2\sigma^2)], \quad (1)$$

where f approximates dN/dE, E_{ion} is the ion kinetic energy, and A, μ, and σ are unique fitting parameters for each curve. These curve fits are included as broken gray lines in Fig. 4, and the closeness of each fit is quantified in Table II. Similar fitting functions along with their physical basis are described in previous experimental and theoretical studies.[23,24] Using the curve fits to the data at each laser wavelength, the average charge state and average ion energy, as well as the ion

TABLE I. Laser parameters used in the experiments. The boundaries of the focal diameter are defined where the intensity in the focal plane is equal to $(1/e^2)$ of its maximum value. The focusing lens in each experiment is planoconvex with focal length f and f/No. given below.

Wavelength [μm]	Pulse duration (ns)	Pulse energy (mJ)	Focal diameter [μm]	f (cm)	f/No.	Resultant laser intensity [W/cm^2]
1.064	7	120	80	30	f/15	3.4×10^{11}
10.6	85	120	100	6	f/6	1.8×10^{10}

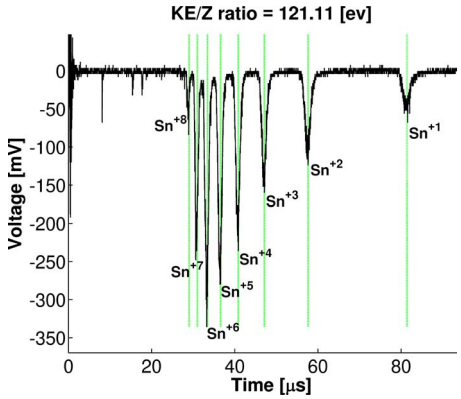

FIG. 3. (Color online) Typical waveform generated by the electrostatic ion energy analyzer using the CO_2 laser. The curve is the data and the vertical lines represent theoretical time-of-flight markers where Sn ions are expected to arrive at the CEM. The additional peaks seen in the data before Sn^{+8} represent H, C, N, or O ions from the thin impurity layer on the surface of the target.

concentration and peak ion energy for each charge state can all be calculated, results are found in Table II.

III. DISCUSSION OF EXPERIMENTAL RESULTS

Several general features can be summarized from the experimental results. First, the increase in laser wavelength increases the maximum charge state measured far away from the laser plasma source. Interestingly, as laser intensity is increased beyond the threshold given in the introduction ($10^{15}/\lambda^2$ $W/cm^2/\mu m^2$), the opposite is true, i.e., an increase in laser wavelength reduces the maximum ion charge state far from the laser plasma source.[26,27] This occurs due to the production of a suprathermal electron population at high laser intensities through resonant and nonlinear laser absorption processes. The temperature of these electrons scales with the product $I\lambda^2$, where I is the laser intensity, and these electrons do not contribute efficiently to ionization.[28] At the moderate laser intensities of the present experiments, a single thermal population of electrons is present and the initial electron density in the corona will approximately equal the critical density, n_{cr}. For the Nd:YAG LPP $n_{cr} \approx 10^{21}$ cm^{-3}, and for the CO_2 LPP $n_{cr} \approx 10^{19}$ cm^{-3}. The lower initial electron density of the CO_2 LPP has a significant effect on the recombination processes during and after the laser pulse. The two mechanisms of recombination in the laser plasmas discussed here include three-body recombination and radiative recombination.[29,30] In both processes, a free electron recombines with an ion and a third body (a photon in radiative recombination, a free electron in three-body recombination) is required to conserve energy. A criterion can be derived using the rates for both processes determining which of the two mechanisms is dominant.[31] If the plasma electron density, electron temperature, T_e, and average charge state, $\bar{Z}$, satisfy the relation

$$(n_e/\mathrm{cm}^{-3}) \gg (3 \times 10^{13})(T_e/\mathrm{eV})^{3.75}/\bar{Z}, \tag{2}$$

then three-body recombination is the dominant mechanism. During the laser pulse, this inequality is satisfied for the Nd:YAG LPP, but not for the CO_2 LPP. After the laser pulse, when T_e begins to decay, three-body recombination will quickly become the dominant process for both laser plasmas. Since the rate of three-body recombination will depend on the density of free electrons, the laser plasma with the lower initial electron density will experience less recombination. Thus, for the CO_2 LPP higher charge state ions should be found far away from the laser plasma source, as observed in the experiments. Numerical simulations discussed subsequently support this argument.

The initial electron temperature, T_e, can be estimated from the ion properties through an expression derived in a hydrodynamic model of laser plasma interactions in a similar parameter regime, as discussed in Puell.[32] The relation is given by

$$E_a = 5(\bar{Z}+1)T_e, \tag{3}$$

where E_a is the average ion energy, and has been applied by several authors in interpretation of data from ion probes.[19,31] From Eq. (3) and the values in Table II, T_e is estimated as 37 and 57 eV for the CO_2 and Nd:YAG LPP, respectively. However, the theory in Puell assumes that E_a is evaluated far from the laser plasma source along the target normal, whereas in the experiments E_a is measured far from the laser plasma source but at an angle of 51° with respect to the target normal. It is well know from previous studies that all ion energies are peaked along the target normal, so that ion energies measured at approximately 45° from the target normal are a factor of a few less than those measured along the target normal.[33,34] In addition, the theory in Puell assumes $\bar{Z}$ is evaluated at a distance from the target surface equal to the laser focal radius, whereas in the experiments $\bar{Z}$ is measured

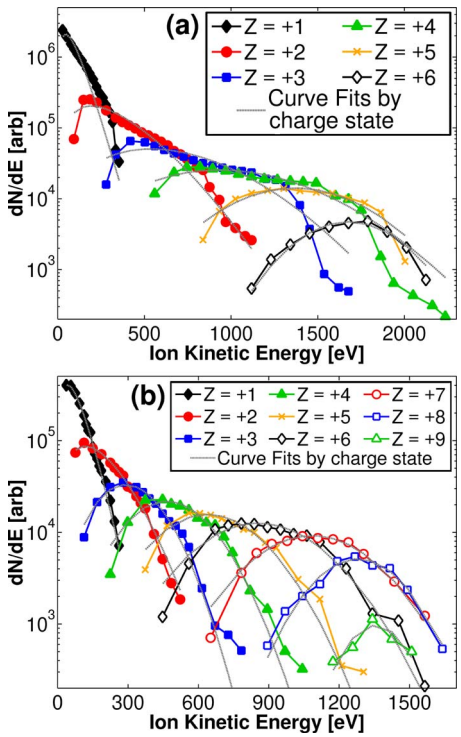

FIG. 4. (Color online) Charge state resolved ion energy distributions from Sn plasma generated with (a) Nd:YAG laser radiation and (b) CO_2 laser radiation, including curve fits for each charge state.

TABLE II. Ion properties calculated from the data and curve fits of Fig. 4. The closeness of the approximation of f to dN/dE can be quantified by the coefficient of determination, R^2, defined, e.g., in Rao.[25] The peak ion energies are the maxima of the curve fits. These ion properties are used subsequently in the discussion section to estimate the initial electron temperature and elucidate the mechanism of ion acceleration.

Wavelength [μm]	Ions	R^2 (%)	Ion concentration (%)	$\bar{Z}$	Peak ion energy (eV)	Average ion energy (eV)
1.064	Sn^{+1}	94.6	59.3	1.8	45	792
	Sn^{+2}	88.3	20.8		191	
	Sn^{+3}	87.9	10.0		536	
	Sn^{+4}	95.0	6.4		931	
	Sn^{+5}	98.3	2.9		1 369	
	Sn^{+6}	99.0	0.7		1 677	
10.6	Sn^{+1}	99.8	40.1	2.7	41	680
	Sn^{+2}	99.1	20.2		116	
	Sn^{+3}	98.4	10.0		289	
	Sn^{+4}	96.3	8.3		463	
	Sn^{+5}	97.3	7.3		637	
	Sn^{+6}	97.1	6.9		854	
	Sn^{+7}	99.1	4.9		1 084	
	Sn^{+8}	98.3	2.1		1 280	
	Sn^{+9}	95.8	0.3		1 356	

far from the laser plasma source. The effect of recombination during plasma expansion into vacuum is known to reduce $\bar{Z}$ by a factor of a few, this topic is treated in several previous studies as well as in the numerical simulations discussed subsequently.[35–37] Accordingly, the order of magnitude estimates of T_e and the qualtitative observation that T_e is higher for the Nd:YAG LPP obtained by using Eq. (3) with the experimental values for $\bar{Z}$ and E_a should still be correct.

The mechanism of ion acceleration can be inferred from a plot of the peak ion energies given in Table II as a function of charge state, as seen in Fig. 5. Similar features observed in both curves indicate the ion acceleration mechanism is independent of laser wavelength. Specifically, the peak ion energies increase approximately linearly as a function of charge state and all ion energies greatly exceed the initial thermal electron temperature. These effects have been noted before from plasma produced by ruby and Nd:YAG lasers in a similar parameter regime, however the authors could not find any experimental data showing these features at the 10.6 μm CO_2 laser wavelength.[38–40]

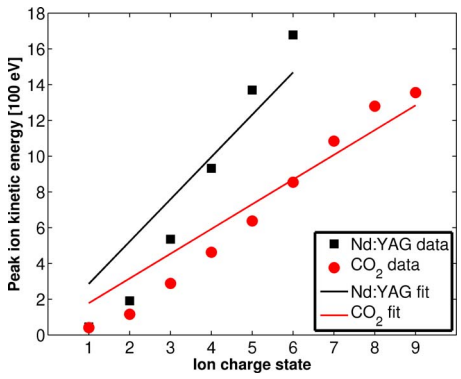

FIG. 5. (Color online) Peak ion energy as a function of charge state from Sn plasma produced by Nd:YAG and CO_2 lasers. Equation (5) is fit to the data at both laser wavelengths. The coefficients of determination, R^2, of the Nd:YAG and CO_2 curve fits are 87% and 93%, respectively.

An acceleration mechanism leading to the observed features in the ion spectra is the electrostatic model.[39,41] Here, electrons heated by the laser through inverse bremsstrahlung transfer energy to ions through collisions on the scale of the electron ion thermalization time, τ_{ei}, given by

$$(\tau_{ei}/s) \approx 3.5 \times 10^8 \frac{(A/\text{amu})(T_e/\text{eV})^{3/2}}{\bar{Z}(n_e/\text{cm}^{-3})\ln \Lambda}, \tag{4}$$

where A is the atomic mass (118.71 amu for Sn) and $\ln \Lambda$ is the Coulomb logarithm ($\approx$5 for laser plasma).[42] Because τ_{ei} will be much shorter than the laser pulse duration, electrons and ions obtain equal thermal temperatures during the laser pulse but due to the mass difference the electrons obtain much higher velocities. The electrons then escape the plasma volume thereby creating an electrostatic field which accelerates ions proportional to their charge. As this process repeats several times during the laser pulse, the resultant ion kinetic energies are typically many times the initial thermal electron temperature, as observed in the experiments. A scaling law with physical significance from the electrostatic model is given by

$$E_{ion} = nZT + T, \tag{5}$$

where E_{ion} is in electron volt, Z is the charge state, and T is the initial electron and ion thermal temperatures (assumed equal) in electron volt.[41] The first term (nZT) represents the repetition of the acceleration process n times during the laser pulse and the second term (T) represents the conversion of thermal electron temperature into ion kinetic energy through expansion. A least squares fit of Eq. (5) to the experimental data at both laser wavelengths is included as a solid line in Fig. 5, the R^2 value quantifying the closeness of each fit is given in the caption. The fitting parameters n and T for the Nd:YAG curve fit are 4.7 and 50 eV, whereas the fitting parameters for the CO_2 curve fit are 3.5 and 40 eV. The effect of recombination during plasma expansion into vacuum,

which is not taken into account in the electrostatic model, prevents better quantitative agreement.

The laser intensities in the two experiments were different (1.8×10^{10} W/cm^2 for the CO_2 LPP and 3.4×10^{11} W/cm^2 for the Nd:YAG LPP), and were chosen such that CE was optimal in each case (3% for the CO_2 LPP and 2% for the Nd:YAG LPP). A significant amount of theoretical work within the EUV x-ray source community has converged on the plasma parameters which optimize CE (see White *et al.*[6] and Refs. 1–12 therein), these being electron temperature of 30–40 eV and electron density of 10^{19} cm^{-3}. Thus, both laser plasmas studied here contain some region with this combination of plasma parameters. The region with the optimal plasma parameters for the CO_2 LPP is the hottest region of the plasma, as the critical density at this wavelength ($\approx10^{19}$ cm^{-3}) is equal to the optimal electron density. In the case of the Nd:YAG LPP, the critical density ($\approx10^{21}$ cm^{-3}) must decay by two orders of magnitude to reach the optimal electron density. Accordingly, the temperature of the Nd:YAG LPP must also decay from its initial value at the critical density to reach the optimal electron temperature, as temperature and density in an LPP decay simultaneously in space.[31] By this argument, the initial electron temperature of the Nd:YAG LPP should be higher than the optimal temperature. The estimate of 50–60 eV inferred from the ion probe data is in agreement.

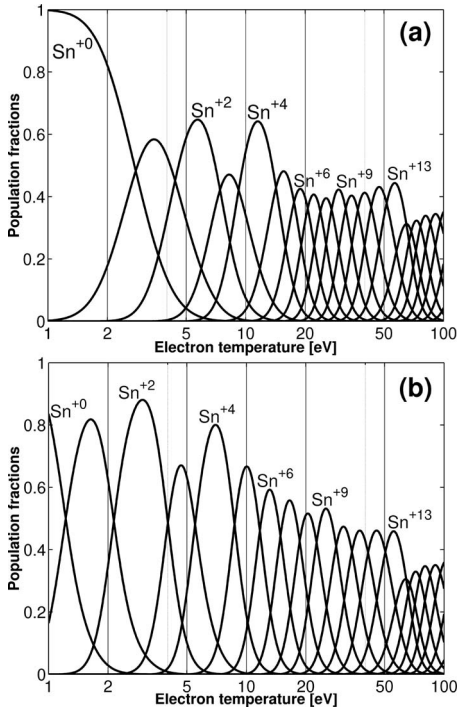

FIG. 6. Collisional-radiative steady state calculations. The population fractions for each charge state of Sn are given as a function of electron temperature at a constant electron density of (a) 10^{21} cm^{-3} and (b) 10^{19} cm^{-3}.

IV. NUMERICAL SIMULATION

Numerical simulations of plasma expansion into vacuum from an assumed initial state have been used extensively in previous laser plasma studies to study the effects of recombination and to explain measurements of charge state distributions made far away from the laser plasma source.[35–37] An adaptation of these codes was used here to support the conclusions from the experimental results.

The initial ion charge state distributions used in the code were calculated from a collisional-radiative steady state model, as described in Colombant and Tonon.[43] Here, a set of equations are solved determining the fractional population of each ion species as a function of electron temperature at a constant electron density. These equations satisfy the steady-state condition for n_Z, the number density of charge state Z, given by

$$\frac{dn_Z}{dt} = n_e n_{Z-1} S_{Z-1} + n_e n_{Z+1} \beta_{Z+1} - n_e n_Z (S_Z + \beta_Z) = 0, \quad (6)$$

where the quantities S_Z and β_Z represent the total ionization and recombination rates, respectively. These rates, found in the original reference, depend on electron temperature, electron density, and the ionization potential and equivalent number of outer shell electrons for each charge state. Measured and calculated ionization potentials for all charge states of Sn are tabulated in Carlson *et al.*[44] The collisional-radiative steady state model is solved at the critical density of the Nd:YAG LPP, 10^{21} cm^{-3} and at the critical density of the CO_2 LPP, 10^{19} cm^{-3}, results are given in Figs. 6(a) and 6(b), respectively. The initial ion charge state distributions used in the code correspond to the population fractions at 60 eV from the data of Fig. 6(a), and at 40 eV from the data of Fig. 6(b), these initial distributions along with the average charge state in each case are given in Table III.

The simulation begins at a time t_0 after which a few electron ion thermalization times have elapsed, so that $T_e = T_i$ can be assumed initially. Equation (4) for τ_{ei} with the electron temperature, electron density, and average charge state from Table III gives $\tau_{ei}=290$ ps for the Nd:YAG LPP, and $\tau_{ei}=19$ ns for the CO_2 LPP. The simulations begin at twice these values. The laser plasma expands isothermally during the laser pulse, therefore the electron temperature is held constant in the simulation from t_0 until the end of the laser pulse. The plasma expansion is assumed spherical for all time, so that at any instant of time the plasma radius, R,

TABLE III. Initial ion population fractions from the collisional-radiative steady state model. The initial electron density in the simulations is assumed to equal the critical density.

λ [μm]	n_{cr} [cm^{-3}]	T_e (eV)	Population fractions								$\bar{Z}$
			+9	+10	+11	+12	+13	+14	+15	+16	
1.064	10^{21}	60			0.02	0.17	0.41	0.27	0.10	0.02	13.3
10.6	10^{19}	40	0.01	0.14	0.42	0.35	0.07				11.3

will be given by $R=c_S t$, where c_S is the constant expansion speed and t is the time variable. The expansion speed is assumed to equal the plasma sound speed, $c_S=\sqrt{\bar{Z}T_e/M_i}$, where M_i is the ion mass. Using the values in Table III, the sound speed is 2.5×10^6 and 1.9×10^6 cm/s for the Nd:YAG and CO_2 LPP, respectively.

The ion distribution for all time is calculated using rate equations for each ion species, given by

$$\frac{dN_k}{dt}=\left(\frac{dN_k}{dt}\right)_c+\left(\frac{dN_k}{dt}\right)_r+\left(\frac{dN_k}{dt}\right)_i, \tag{7}$$

where N_k is the number of ions of charge state k at any time. The first term represents the rate of change due to collisional three-body recombination, the second term due to radiative recombination, and the third term due to electron impact ionization. If Z_{max} charge states are included in the code, then Eq. (7) represents $Z_{max}+1$ equations, in order to include the neutral species ($k=0$). The rate of three-body recombination, radiative recombination, and electron-impact ionization are given in Gurevich and Pitaevskii,[29] Allen,[30] and McWhirter,[45] respectively. Using these rates, the terms in Eq. (7) are then given by

$$\left(\frac{dN_k}{dt}\right)_c=(8.75\times10^{-27})n_e^2T_e^{-9/2}[(k+1)^3N_{k+1}-k^3N_k], \tag{8}$$

$$\left(\frac{dN_k}{dt}\right)_r=(2.7\times10^{-13})n_eT_e^{-3/4}[(k+1)^2N_{k+1}-k^2N_k], \tag{9}$$

$$\left(\frac{dN_k}{dt}\right)_i=(2.4\times10^{-6})n_eT_e^{1/4}\left[\frac{\zeta_{k-1}}{I_{k-1}^{7/4}}\exp\left(-\frac{I_{k-1}}{T_e}\right)N_{k-1}-\frac{\zeta_k}{I_k^{7/4}}\exp\left(-\frac{I_k}{T_e}\right)N_k\right], \tag{10}$$

where I_k is the ionization potential in electron volt and ζ_k is the equivalent number of outershell electrons for the charge state k. The units of n_e are cm^{-3} and the units of T_e are electron volt. In Eqs. (8) and (9), N_k can increase through recombination in the upper state, whereas in Eq. (10) N_k can increase through ionization in the lower state. At each time step, the number of electrons, N_e, is determined through the plasma neutrality condition,

$$N_e=\sum_{k=1}^{Z_{max}}kN_k. \tag{11}$$

The equation for the time evolution of electron temperature is given by[42]

$$\frac{dT_e}{dt}=-\left(2\frac{T_e}{t}\right)+\frac{T_i-T_e}{\tau_{ei}}-\left(\frac{2}{3}\times\frac{Q}{1+N_e/N}\right), \tag{12}$$

where N is the total number of heavy particles,

$$N=\sum_{k=0}^{Z_{max}}N_k. \tag{13}$$

The solution of Eq. (12) if only the first term on the right-hand-side were present would be $T_e\sim t^{-2}$, which just describes the adiabatic expansion of plasma into vacuum.[31] The second term in Eq. (12) is due to temperature relaxation and is necessary when the electron ion thermalization time exceeds the simulation time, which occurs late in the simulations studied here. The third term in Eq. (12) represents the contribution of the excess energy in collisional recombination or ionization. During electron impact ionization, the free electron loses energy. The inverse process, three-body recombination, thus transfers energy to the free electron. Because the rate of electron impact ionization is proportional to $\exp(-I_k/T_e)$, this process becomes negligible as T_e decays to a value much less than the first ionization potential. However, as T_e decays the rate of three-body recombination increases dramatically due to its $T_e^{-9/2}$ scaling. The result of the excess energy given to free electrons during three-body recombination is to slow the adiabatic decay of T_e to a decay of approximately $T_e\sim t^{-1}$, this topic has been treated theoretically before.[35,46] The quantity Q thus depends on the rates of collisional recombination and ionization as well as the excess energy, E^*, in each event, and is given by

$$Q=\frac{1}{N}\sum_{k=1}^{Z}E_k^*\left[\left(\frac{dN_k}{dt}\right)_c+\left(\frac{dN_k}{dt}\right)_i\right], \tag{14}$$

where E^* is derived originally by Kuznetsov and Raizer[35] and has since been applied by several authors in their calculations.[36,37,42] Finally, an equation for the decay of ion temperature is required due to the inclusion of the temperature relaxation term. This is just

$$\frac{dT_i}{dt}=-\left(2\frac{T_i}{t}\right)-\frac{T_i-T_e}{\tau_{ei}}. \tag{15}$$

The set of Eqs. (8)–(15) represent a nonlinear set of first order differential equations and were integrated using a stiff algorithm. Similar versions of the code discussed here are described in Voronov and Chernyshev[37] to model the decay of a fully ionized Al plasma, and in Zel'dovich and Razier[42] to model the decay of a H plasma. As a check of our work we replicated the results from these previous studies first.

The results of the numerical simulations are shown in Fig. 7(a) for the Nd:YAG LPP and in Fig. 7(b) for the CO_2 LPP. As seen in the figures, the lower initial electron density of the CO_2 LPP leads to the presence of higher charge state ions after the effects of recombination have ceased, as observed in the experiments through measurements of the charge-state resolved ion energy distributions far from the laser plasma source. The impact of the third term in Eq. (12) was indeed to slow the adiabatic decay of electron temperature almost to $T_e\sim t^{-1}$, as predicted in theoretical works.[35,46] Without the third term in Eq. (12), the plasma always recombined completely, i.e., the preservation of charge state far from the laser plasma source is a result of the excess energy of three-body recombination.

In both experiment and simulation, the lower initial electron density of the CO_2 LPP leads to the presence of higher charge state ions far from the laser plasma source, as compared to the Nd:YAG LPP. The angular dependence of the ion properties was not taken into account in the simulation in order to avoid multidimensional complexity, however the plasma is known to have an anisotropic distribution which

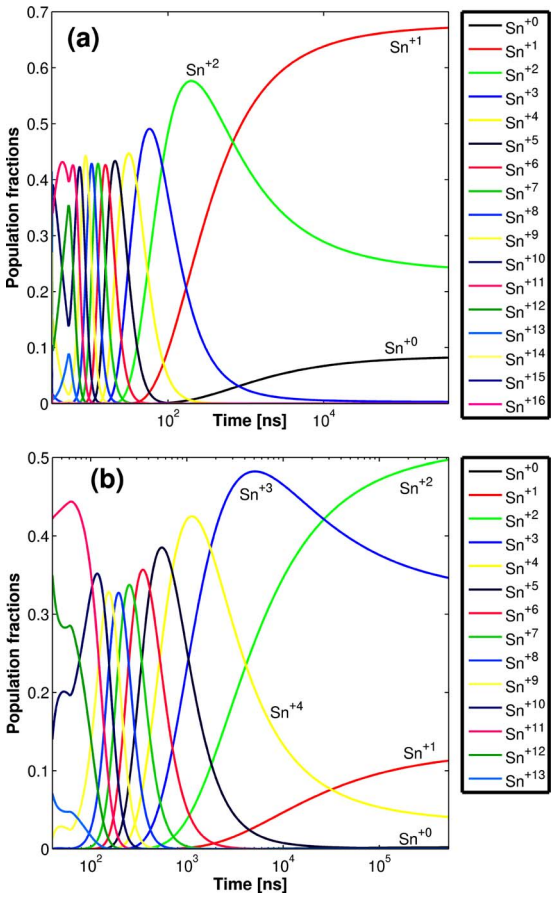

FIG. 7. (Color online) Numerical simulation of the time evolution of ion and neutral population fractions from Sn plasma with an initial electron density of (a) 10^{21} cm^{-3} and (b) 10^{19} cm^{-3}.

depends upon the laser parameters. The dimensionality of the expansion is set approximately by the ratio of the laser focal diameter (d_S) to the initial density scale length ($l_S = n_e/|\nabla n_e|$); when this ratio is large the plasma exhibits one-dimensional (1D) expansion. For the Nd:YAG LPP, the density scale length is about 100 μm, whereas for the CO_2 LPP recent investigations have shown the scale length to be about 50 μm.[47,48] The expansion ratio (d_S/l_S) is then 0.8 and 2 for the Nd:YAG and CO_2 LPP, respectively, so the CO_2 LPP should exhibit less dimensionality in its expansion. The opposite was observed in an experimental comparison of the angular distribution of ion energies from Nd:YAG and CO_2 LPP, i.e., the distribution from the CO_2 LPP was more broad.[49] However, the intensity distribution at the focus of the CO_2 laser in that experiment was annular due to an unstable cavity, and this was explained to lead to the enhanced lateral expansion. The intensity distribution of the CO_2 laser in the experiments discussed here is measured directly and is nearly Gaussian ($M^2 \approx 1.3$, see Ref. 17 for images of the focused beam), so the expectation of less dimensionality in the expansion of the CO_2 LPP should be correct. Accordingly, if the ion energy distributions were measured along the target normal instead of at a constant angle of 51°, the differences should be even more pronounced as compared to the experimental observations.

Finally, the numerical model could only verify the qualitative features of the experiments and did not quantitatively reproduce the results due to the assumptions in the code. Specifically, the code follows variations in plasmas parameters in time only, i.e., it is zero-dimensional. Of course, different components of the plasma move at different speeds, and this separation allows the plasma to preserve higher charge states than those dictated by the simulation. A 1D version of the code discussed here has been used to study laser plasma in a similar parameter regime with the conclusion that the lack of accurate initial conditions will always prevent quantitative results.[50] In other studies, initial conditions were either taken from experimental measurements or chosen to fit the simulation results with the data, which removes any predictive capability.[51,52] Only simulations incorporating two-dimensional hydrodynamics to properly model the initial ionization and laser absorption, along with collisional-radiative rate equations including the excess energy released in three-body recombination are able to reproduce experimental measurements of ion distributions quantitatively.[46]

V. CONCLUSIONS

The charge-state resolved ion energy distributions from Sn plasma produced by 1.064 μm Nd:YAG and 10.6 μm CO_2 lasers were studied. The effect of varying the laser wavelength by an order of magnitude was to vary the initial electron density of the plasma by approximately two orders of magnitude. At the longer laser wavelength, this resulted in the preservation of higher charge states after the effects of recombination had ceased. This phenomenon was observed experimentally and in numerical simulations. By applying a hydrodynamic model to the data, and by curve-fitting a scaling law from the electrostatic model of ion acceleration to the data, it was concluded that the initial electron temperature of the Nd:YAG LPP should be higher as compared to the CO_2 LPP. The initial electron temperature of the Nd:YAG LPP and CO_2 LPP was estimated as 60 and 40 eV, respectively, and these values were used as initial conditions in the numerical simulations.

ACKNOWLEDGMENTS

This work was supported by KLA-Tencor Corporation and the University of California under the UC Industry-University Cooperative Research Program.

[1] P. Mulser, R. Sigel, and S. Witkowski, Phys. Rep. **6**, 187 (1973).
[2] J. M. Dawson, Phys. Fluids **7**, 981 (1964).
[3] N. Basov, G. Vergunova, E. Gamalit, V. Gasilov, N. Demchenko, A. Isakov, A. Kologrivov, Y. Merkuliev, V. Rozanov, A. Samarsky, G. Sklizkov, V. Tishkin, A. Favorsky, and A. Shikanov, JETP Lett. **84**, 564 (1983).
[4] R. H. Stulen and D. W. Sweeney, IEEE J. Quantum Electron. **35**, 694 (1999).
[5] R. C. Spitzer, R. L. Kauffman, T. Orzechowski, D. W. Phillion, and C. Cerjan, J. Vac. Sci. Technol. B **11**, 2986 (1993).
[6] J. White, P. Dunne, P. Hayden, F. O'Reilly, and G. O'Sullivan, Appl. Phys. Lett. **90**, 181502 (2007).
[7] S. Fujioka, H. Nishimura, K. Nishihara, A. Sasaki, A. Sunahara, T. Okuno, N. Ueda, T. Ando, Y. Tao, Y. Shimada, K. Hashimoto, M. Yamaura, K. Shigemori, M. Nakai, K. Nagai, T. Norimatsu, T. Nishikawa, N. Miyanaga, Y. Izawa, and K. Mima, Phys. Rev. Lett. **95**, 235004 (2005).
[8] A. Cummings, G. O'Sullivan, P. Dunne, E. Sokell, N. Murphy, and J. White, J. Phys. D **38**, 604 (2005).

[9]Y. Tao, S. S. Harilal, M. S. Tillack, K. L. Sequoia, B. O'Shay, and F. Najmabadi, Opt. Lett. **31**, 2492 (2006).
[10]S. S. Harilal, M. S. Tillack, Y. Tao, B. O'Shay, R. Paguio, and A. Nikroo, Opt. Lett. **31**, 1549 (2006).
[11]Y. Tao, M. S. Tillack, K. L. Sequoia, R. A. Burdt, S. Yuspeh, and F. Najmabadi, Appl. Phys. Lett. **92**, 251501 (2008).
[12]Y. Ueno, G. Soumagne, A. Sumitani, A. Endo, and T. Higashiguchi, Appl. Phys. Lett. **91**, 231501 (2007).
[13]U. Stamm, J. Phys. D **37**, 3244 (2004).
[14]S. S. Harilal, B. O'Shay, Y. Tao, and M. S. Tillack, Appl. Phys. B: Lasers Opt. **86**, 547 (2007).
[15]M. Richardson, C. S. Koay, K. Takenoshita, C. Keyser, and M. Al-Rabban, J. Vac. Sci. Technol. B **22**, 785 (2004).
[16]R. A. Burdt, S. Yuspeh, K. L. Sequoia, Y. Tao, M. S. Tillack, and F. Najmabadi, J. Appl. Phys. **106**, 033310 (2009).
[17]Y. Tao, M. S. Tillack, N. Amin, R. A. Burdt, S. Yuspeh, N. M. Shaikh, and F. Najmbadi, Rev. Sci. Instrum. **80**, 123503 (2009).
[18]E. Woryna, P. Parys, J. Wolowski, and W. Mroz, Laser Part. Beams **14**, 293 (1996).
[19]S. Denus, J. Farny, Z. Wereszczynski, J. Wolowski, and E. Woryna, J. Tech. Phys. **18**, 25 (1977).
[20]T. S. Green, Plasma Phys. **12**, 877 (1970).
[21]E. Flaxer, Meas. Sci. Technol. **17**, N37 (2006).
[22]M. Krems, J. Zirbel, M. Thomason, and R. D. Dubois, Rev. Sci. Instrum. **76**, 093305 (2005).
[23]R. Kelly and R. W. Dreyfus, Surf. Sci. **198**, 263 (1988).
[24]G. J. Tallents, Opt. Commun. **37**, 108 (1981); **38**, 448(E) (1981).
[25]C. R. Rao, *Linear Statistical Interference and Its Applications*, 2nd ed. (Wiley, New York, 1973).
[26]L. Láska, K. Jungwirth, B. Kralikova, J. Krasa, M. Pfeifer, K. Rohlena, J. Skala, J. Ullschmied, J. Badziak, P. Parys, J. Wolowski, E. Woryna, S. Gammino, L. Torrisi, F. P. Boody, and H. Hora, Plasma Phys. Controlled Fusion **45**, 585 (2003).
[27]S. J. Gitomer, R. D. Jones, F. Begay, A. W. Ehler, J. F. Kephart, and R. Kristal, Phys. Fluids **29**, 2679 (1986).
[28]D. W. Forslund, J. M. Kindel, and K. Lee, Phys. Rev. Lett. **39**, 284 (1977).
[29]A. V. Gurevich and L. P. Pitaevskii, Sov. Phys. JETP **19**, 870 (1964).
[30]C. W. Allen, *Astrophysical Quantities* (Athlone, London, 1955), p. 90.
[31]P. T. Rumsby and J. W. M. Paul, Plasma Phys. **16**, 247 (1974).
[32]H. Puell, Z. Naturforsch. B **25a**, 1807 (1970).
[33]L. Láska, J. Krasa, M. Pfeifer, K. Rohlena, S. Gammino, L. Torrisi, L. Ando, and G. Ciavola, Rev. Sci. Instrum. **73**, 654 (2002).
[34]A. Thum-Jager and K. Rohr, J. Phys. D **32**, 2827 (1999).
[35]N. M. Kuznetsov and Y. P. Raizer, J. Appl. Mech. Tech. Phys. **6**, 6 (1965).
[36]M. Mattioli, Plasma Phys. **13**, 19 (1971).
[37]G. S. Voronov and L. E. Chernyshev, Sov. Phys. Tech. Phys. **18**, 940 (1974).
[38]B. E. Paton and N. R. Isenor, Can. J. Appl. Physiol. **46**, 1237 (1968).
[39]Y. Bykovskii, N. Degtyarenko, V. Dymovich, V. Elesin, Y. Kozyrev, B. Nikolaev, S. Ryzhikh, and S. Sil'nov, Sov. Phys. Tech. Phys. **14**, 1269 (1970).
[40]R. Dinger, K. Rohr, and H. Weber, J. Phys. D **13**, 2301 (1980).
[41]W. Demtroder and W. Jantz, Plasma Phys. **12**, 691 (1970).
[42]Y. B. Zel'dovich and Y. P. Razier, in *Physics of Shock Waves and High-Temperature Hydrodynamic Phenomena*, edited by W. D. Hayes and R. F. Probstein (Dover, New York, 2002).
[43]D. Colombant and G. F. Tonon, J. Appl. Phys. **44**, 3524 (1973).
[44]T. A. Carlson, C. W. Nestor, N. Wasserman, and J. D. McDowell, At. Data **2**, 63 (1970).
[45]R. W. P. McWhirter, *Plasma Diagnostic Techniques* (Academic, New York, 1965), p. 210.
[46]I. V. Roudskoy, Laser Part. Beams **14**, 369 (1996).
[47]Y. Tao, H. Nishimura, S. Fujioka, M. Nakai, T. Okuno, N. Ueda, K. Nishihara, N. Miyanaga, and Y. Izawa, Appl. Phys. Lett. **86**, 201501 (2005).
[48]Y. Tao, M. S. Tillack, S. Yuspeh, R. Burdt, and F. Najmabadi, Hydrodynamic behavior of Sn plasma irradiated with a long CO_2 laser pulse, submitted 2009 (unpublished).
[49]H. Tanaka, A. Matsumoto, K. Akinaga, A. Takahashi, and T. Okada, Appl. Phys. Lett. **87**, 041503 (2005).
[50]I. Kunz, "Interpretation of ion energy spectra of laser plasmas by the recombination model," Ph.D. thesis, Technische Hochschule, 1990.
[51]R. R. Goforth and P. Hammerling, J. Appl. Phys. **47**, 3918 (1976).
[52]G. L. Payne, J. D. Perez, T. E. Sharp, and B. A. Watson, J. Appl. Phys. **49**, 4688 (1978).